



THE UNIVERSITY *of* EDINBURGH

Edinburgh Research Explorer

Structural controls on the location and distribution of CO₂ emission at a natural CO₂ spring in Daylesford, Australia

Citation for published version:

Roberts, JJ, Lepastrier, A, Feitz, AJ, Shipton, ZK, Bell, AF & Karolyt, R 2019, 'Structural controls on the location and distribution of CO₂ emission at a natural CO₂ spring in Daylesford, Australia', *International Journal of Greenhouse Gas Control*, vol. 84, pp. 36-46. <https://doi.org/10.1016/j.ijggc.2019.03.003>

Digital Object Identifier (DOI):

[10.1016/j.ijggc.2019.03.003](https://doi.org/10.1016/j.ijggc.2019.03.003)

Link:

[Link to publication record in Edinburgh Research Explorer](#)

Document Version:

Peer reviewed version

Published In:

International Journal of Greenhouse Gas Control

General rights

Copyright for the publications made accessible via the Edinburgh Research Explorer is retained by the author(s) and / or other copyright owners and it is a condition of accessing these publications that users recognise and abide by the legal requirements associated with these rights.

Take down policy

The University of Edinburgh has made every reasonable effort to ensure that Edinburgh Research Explorer content complies with UK legislation. If you believe that the public display of this file breaches copyright please contact openaccess@ed.ac.uk providing details, and we will remove access to the work immediately and investigate your claim.



1 **Structural controls on the location and distribution of CO₂ emission at a natural CO₂ spring in**
2 **Daylesford, Australia**

3 Jennifer J Roberts¹, Aero Leplastrier², Andrew J Feitz², Zoe K Shipton¹, Andrew F Bell³, Rūta Karolytė³

4 ¹Department of Civil and Environmental Engineering, University of Strathclyde, Glasgow G1 1XJ,
5 Scotland, UK

6 ²Geoscience Australia, GPO Box 378, Canberra ACT 2601, Australia

7 ³School of Geosciences, University of Edinburgh, Grant Institute, Edinburgh, EH9 3FE, Scotland, UK

8

9 **Abstract**

10 Secure storage of CO₂ is imperative for carbon capture and storage technology, and relies on a
11 thorough understanding of the mechanisms of CO₂ retention and leakage. Observations at CO₂
12 seeps around the world find that geological structures at a local and regional scale control the
13 location, distribution and style of CO₂ emission. Bedrock-hosted natural CO₂ seepage is found in the
14 Daylesford region in Victoria, Australia, where many natural springs contain high concentrations of
15 dissolved CO₂. Within a few meters of the natural Tipperary Mineral Spring, small CO₂ bubble
16 streams are emitted from bedrock into an ephemeral creek. We examine the relationship between
17 structures in the exposed adjacent outcropping rocks and characteristics of CO₂ gas leakage in the
18 stream, including CO₂ flux and the distribution of gas emissions. We find that degassing is clustered
19 within ~1 m of a shale-sandstone geological contact. CO₂ emission points are localised along bedding
20 and fracture planes, and concentrated where these features intersect. The bubble streams were
21 intermittent, which posed difficulties in quantifying total emitted CO₂. Counterintuitively, the
22 number of bubble streams and CO₂ flux was greatest from shale dominated rather than the
23 sandstone dominated features, which forms the regional aquifer. Shallow processes must be
24 increasing the shale permeability, thus influencing the CO₂ flow pathway and emission locations.
25 CO₂ seepage is not limited to the pool; leakage was detected in subaerial rock exposures, at the
26 intersection of bedding and orthogonal fractures.

27 These insights show the range of spatial scales of the geological features that control CO₂ flow.
28 Microscale features and near surface processes can have significant effect on the style and location
29 and rates of CO₂ leakage. The intermittency of the bubble streams highlights challenges around
30 characterising and monitoring CO₂ stores where seepage is spatially and temporally variable. CCS
31 monitoring programmes must therefore be informed by understanding of shallow crustal processes
32 and not simply the processes and pathways governing CO₂ fluid flow at depth. Understanding how
33 the CO₂ fluids leaked by deep pathways might be affected by shallow processes will inform the
34 design of appropriate monitoring tools and monitoring locations.

35 **Keywords:** CO₂ flux; CO₂ storage; mineral springs; CO₂ leakage; natural analogues

36

37 **Introduction**

38 Carbon Capture and Storage (CCS) is an important component of CO₂ emission reduction strategies
39 (OECD/IEA, 2015). Legislation and guidelines developed for CCS have set performance requirements
40 to minimise leakage risk (Dixon et al., 2015). For CCS to be an effective mitigation strategy the
41 injected CO₂ must remain securely in the subsurface (Schaffer et al., 2013). To avoid CO₂ leakage,
42 site selection criteria must be guided by a thorough understanding of the geological characteristics
43 that are most relevant to site integrity (Carpenter et al., 2011; Pearce and Czernichowski-Lauriol,
44 2004). As such there has been considerable research effort to understand the crustal fluid pathways
45 of CO₂ migrating from depth (Holloway et al. 2007; Oldenburg and Lewicki, 2006; Roberts et al.,
46 2017a). However there have been far fewer studies on fluid pathways in the near-surface. Effective
47 surface monitoring strategies to detect and quantify CO₂ leakage from geologic stores therefore
48 need to include an understanding of how near-surface processes affect leakage expression (Feitz et
49 al., 2014; Jenkins et al., 2015; Roberts et al., 2017b).

50 Studies of natural analogues identify that geological structures, such as faults, govern CO₂ fluid flow
51 on a macroscale (Dockrill and Shipton, 2010; Burnside et al., 2013; Miocic et al., 2016; Roberts et
52 al., 2017a). Fractures are also known to be an important control for fluid flow at meso- and micro-
53 scale e.g. (Bond et al., 2013; 2017; Roberts et al., 2014), and the presence of fractures have
54 complicated injection operations at pilot CCS sites (Rinaldi and Rutqvist, 2013; Verdon et al., 2013).
55 To date, there has been little focus on the influence of microscale features, such as bedding planes
56 and small fractures within foliated planes, on the surface expression of leaking CO₂—though these
57 features are known to affect geofluid flow (Faulkner et al., 2010; Hippler, 1993; McCay et al., 2018).

58 Further, field experiments designed to mimic CO₂ seepage by controlled CO₂ release at shallow
59 depths have found CO₂ flow pathways are influenced by a number of local factors, and thus the
60 location and style of seepage is difficult to predict (Roberts and Stalker, 2017). Thus, current
61 understanding of the surface processes that govern CO₂ flow is limited. Here, we address this
62 knowledge gap by presenting the characteristics of CO₂ leakage at Tipperary Mineral Spring,
63 Daylesford (Victoria, Australia) where naturally occurring CO₂ seeps from exposed bedrock.

64 **Geology and Hydrology of the Daylesford region**

65 The Daylesford region in the Central Highlands of Victoria hosts over sixty mineral springs that are
66 naturally rich in dissolved CO₂ (Cartwright et al., 2000; Laing, 1977; Shugg, 1996; Wishart and
67 Wishart, 1990). These waters have historically been of economic importance to the region,
68 facilitating commercial water bottling operations, health spas, and tourism (Lawrence, 1969).
69 Although the mineral springs were first described by European settlers in the 1830s (Wishart and
70 Wishart, 1990), mining activities in the Victorian Gold Rush (1850s - 60s) informed much of the
71 current understanding of the geology and hydrology within the Daylesford area.

72 The regional geology comprises three principal units: deformed Ordovician turbidites of the
73 Castlemaine Group, Devonian granites, and Quaternary basalts of the Newer Volcanics Province
74 (VandenBerg, 1978) (Figure 1). The turbidites consist of greenschist facies slates, shales, and
75 sandstones in a 4500 m thick flysch sequence. These were extensively folded, fractured, and faulted
76 in a single deformation event, the Tabberabberan Orogeny, estimated to have caused a 50-70%
77 crustal shortening of this province (Cox et al., 1991a; Gray and Willman, 1991; VandenBerg, 1978;
78 Gray et al., 1991). The timing of the orogeny is constrained by the coeval intrusion of granitoids,
79 which date to the Late Devonian (Richards and Singleton, 1981). The regional structure is now
80 dominated by NNW trending folds that extend up to 100 km in length with wavelengths between
81 10-15 km (Cox et al., 1991a; Gray and Willman, 1991; Lawrence, 1969; VandenBerg, 1978) (Figure
82 1). Shorter subsidiary folds < 10 km length have wavelengths on the order of 150-500 m (Cox et al.,
83 1991a). The compression also developed a series of west-dipping high-angle reverse faults across
84 the region, with a minor set of east-dipping conjugates (Cox et al., 1991a; Gray and Willman, 1991;
85 Shugg, 2009). Fold-associated fractures formed conduits for gold-bearing fluids during the late
86 stages of regional deformation (Cox et al., 1991b). Mining of the Daylesford Gold Field between
87 1853-1951 and coincident underground mapping provided valuable insight into the subsurface
88 structures (Maddicks and Butler, 1981). Mining records show west-dipping faults repeat at 60–120

89 m intervals in the Lower Ordovician sandstone-rich rocks near Daylesford (Shugg, 2009). Faults that
90 cross-cut the metasediments contain fault breccia cemented with quartz (Shugg, 2009), and similar
91 quartz-breccia 'reefs' are also found in anticline crests (Cox et al., 1991b). Reefs in the fold hinges
92 and faults can extend for up to 4 km, and were the target for gold miners (Shugg, 2009). The
93 Ordovician turbidites and Devonian granites are overlain by Newer Volcanic basalts, which form a
94 widespread discontinuous plateau and date from 4.5 Ma to ~4.3 ka, with peak activity around 2.6
95 Ma (Gill, 1964; Mcdougall et al., 1966).

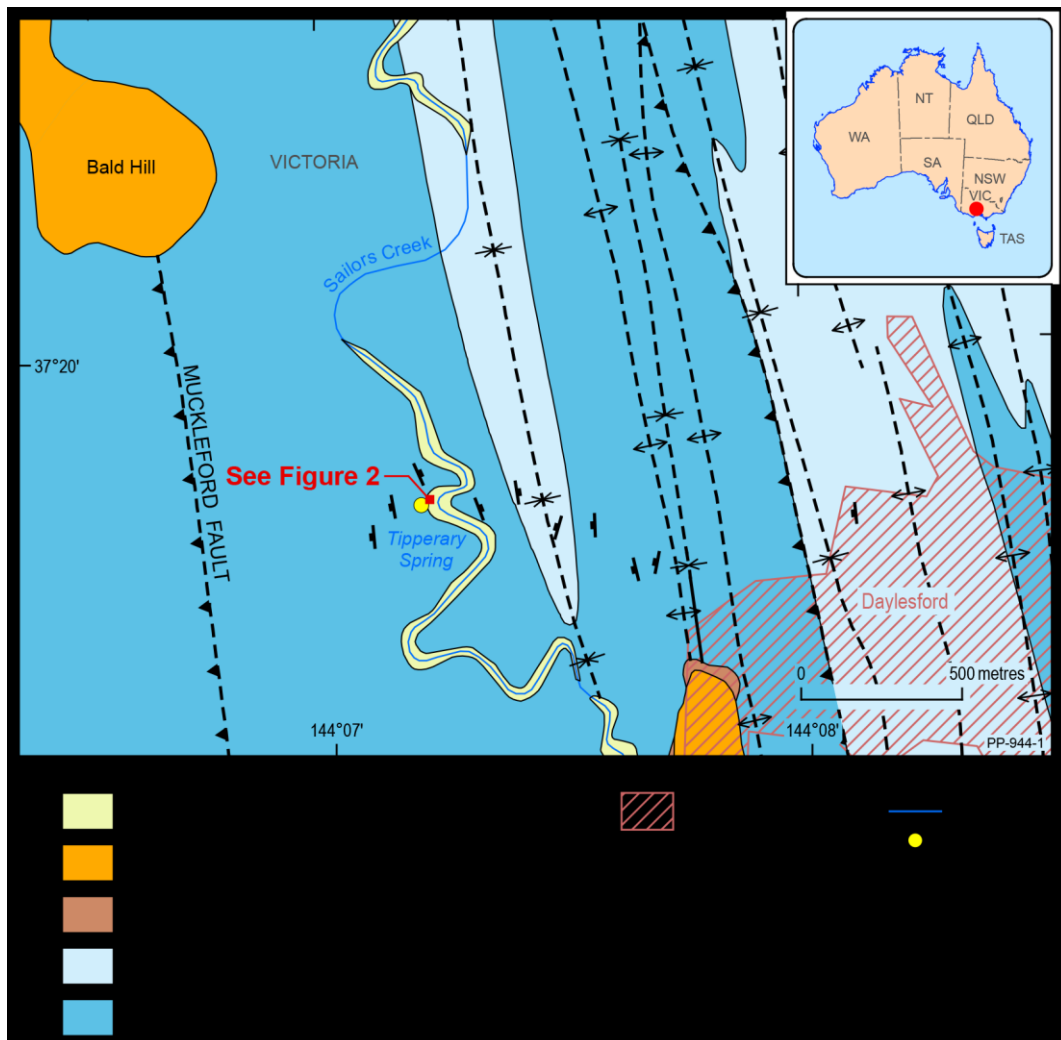
96 The faults, joints, fractures and cleavage developed in the bedrock facilitate groundwater and
97 mineral water circulation (Shugg, 2009). The Ordovician turbidites and Quaternary basalts form
98 regional fractured aquifers. The Ordovician bedrock has two distinct groundwater systems; a
99 shallow fresh groundwater system and a second deeper mineral water system. The two systems mix
100 to varying degrees, especially near the surface expressions of the mineral springs (Shugg, 2004). The
101 CO₂ in the Daylesford Region mineral water is mantle-derived, and so has migrated from a deep-
102 seated source into the Ordovician fractured aquifer (Cartwright et al., 2000; Lawrence, 1969). The
103 mineral waters have a residence time of ~4.5 ka (Cartwright et al., 2002) and are assumed to
104 recharge within the nearby Great Dividing Range, as well as through local volcanics that outcrop at
105 higher elevations in the regional topography (Shugg, 1996).

106 The Daylesford mineral springs are high in calcium, magnesium, and bicarbonates, and so are quite
107 different from typical Australian Na-Cl rich groundwater (Cartwright et al., 2002; Weaver et al.,
108 2006). Individual spring water chemistry has changed little during 20 years of detailed
109 measurements although some springs exhibit mixing with fresh water during discharge (Weaver et
110 al., 2006). The total dissolved CO₂ content of the mineral waters is also consistent across the region
111 (Cartwright et al., 2000; Laing, 1977; Weaver et al., 2006). Spring geochemistry is controlled by fluid-
112 rock interactions facilitated by elevated CO₂ partial pressures (Karolytė et al., 2017), and, because
113 each spring is geochemically unique (Laing, 1977), it is thought that the subsurface catchment
114 feeding each spring is highly heterogeneous (Weaver et al., 2006).

115 *The study area: Tipperary Spring*

116 The Tipperary Mineral Spring is one of 13 springs around the Daylesford township (Wishart and
117 Wishart, 1990). Tipperary Mineral Springs Reserve is located 2.5 km west of Daylesford
118 (37°20'14.8"S 144°07'14.2"E, Figure 1). The spring eye is located on the west bank of Sailors Creek,
119 beneath a footbridge crossing the creek, demarked by the presence of CO₂ gas bubbles into the

120 creek bed. The bubbles are most apparent during the dry season when water level in the creek drops
121 (Shugg and Brumley, 2003). A hand pump on the east side of Sailors Creek draws water from a
122 borehole which was drilled in 2001. The bore encountered a significant flow of gassy mineral water
123 in a highly fractured horizon at 45 m depth, and the borehole casing was pressure cemented in this
124 portion (Shugg and Brumley, 2003). The mineral water is effervescent. Gases dissolved in the
125 mineral waters of the Daylesford region are reported to range from 88.6 – 95.7 % CO₂ with between
126 0.4 – 0.8 % O₂, 3.9 – 10.2 % N₂ and host trace quantities of He and Ne (Cartwright et al., 2000;
127 Lawrence, 1969). The gasses emitted as bubbles at the seep bed are >99% CO₂ (Karolyte et al., in
128 prep). To date, the characteristics of the degassing, flux and distribution of CO₂ seepage at Tipperary
129 have not been studied in detail.



130
131 **Figure 1:** Regional geological map, adapted from (Osborne et al., 2002), showing the main geological and structural
132 features of the region north west of Daylesford, Victoria. The location of our study site, Tipperary Spring, is located along
133 Sailors Creek. **Inset:** Map of Australia, showing the location of Daylesford in red.

134

135 **Methods**

136 Fieldwork at Tipperary was conducted in March 2017, towards the end of the summer when the
137 creek level was low. The fieldwork aimed to collect geological and structural data at the site to
138 observe the style of CO₂ degassing and measure gas fluxes.

139 High precision GPS measurements of bubble locations and outcrop/creek features were taken using
140 an Altus APS3G high precision GNSS survey system for Real Time Kinematic (RTK) position
141 measurements. A base station was set up at each locality and the Rover recorded the UTM
142 coordinates of the feature. The positional accuracy of the RTK equipment is < 1 mm, but human
143 error positioning the RTK will be on the order of < 1 cm. There were some time delays and
144 complications obtaining position measurements due to tree cover and the footbridge which, in
145 addition to the typically sporadic nature of the bubbles streams, meant that the location of the
146 bubble streams was recorded using a local reference grid rather than the RTK. The bubble location
147 error is therefore approximately ~10 cm.

148 CO₂ flux measurements were obtained using a West Systems portable flux system with attached
149 accumulation chamber (type B) and LI-840A CO₂/H₂O gas analyser following the method established
150 by Chiodini et al. (2001). A hollow 50mm PVC pipe frame was attached to the base of the
151 accumulation chamber as a floatation device in order to facilitate flux sampling at the water surface.
152 The base of the accumulation chamber was therefore slightly submerged in water and this change
153 in volume was accounted for when applying the ACK (a conversion factor between ppm/sec
154 (instrument unit) and g/m²/day). ACK temperature and pressure corrections (see Annex A) were
155 made using meteorological measurements recorded at the nearby Ballarat Airport at 10 min
156 intervals (Weatherzone, 2017). Where required, the floating flux chamber was attached to a pole to
157 enable sampling of bubble streams without disturbing the creek sediments.

158 Flux measurements were made at bubbling points. Several readings were also taken at non-bubbling
159 points across the pool to account for background diffuse degassing. The measurement period
160 varied, but generally lasted for 90 seconds or longer, or until the accumulation in the chamber
161 reached a CO₂ concentration of 20,000 ppm (at which point the accuracy of the gas analyser is
162 negatively impacted). Time restraints prevented the quantitative measurement of every mapped
163 bubble point, so our sampling focussed on the most vigorous and continuous bubbling points in the
164 interests of producing the most reliable upper bound estimate of the total CO₂ emission rate. A

165 more detailed discussion of the characteristics and style of the gas emissions at Tipperary is reported
166 in Roberts et al (2018).

167 The presence of 'dry' seeps (CO₂ seepage from rock to atmosphere, not through water) was
168 investigated using a tube connected to a Li-COR 81000A soil gas flux system ('CO₂ sniffer'), allowing
169 CO₂ concentrations of the air to be continuously measured. The inflow tube was used to identify
170 structural features in the outcrop that hosted dry gas seeps.

171 Structural measurements of outcropping bedrock were collected digitally using FieldMove Clino.
172 The area of outcrop and the pool area were calculated from GPS measurements using ArcMap 10.2
173 ©ESRI 2013. Spatial statistical analyses were performed to quantitatively examine seep distributions
174 with respect to geological structures.

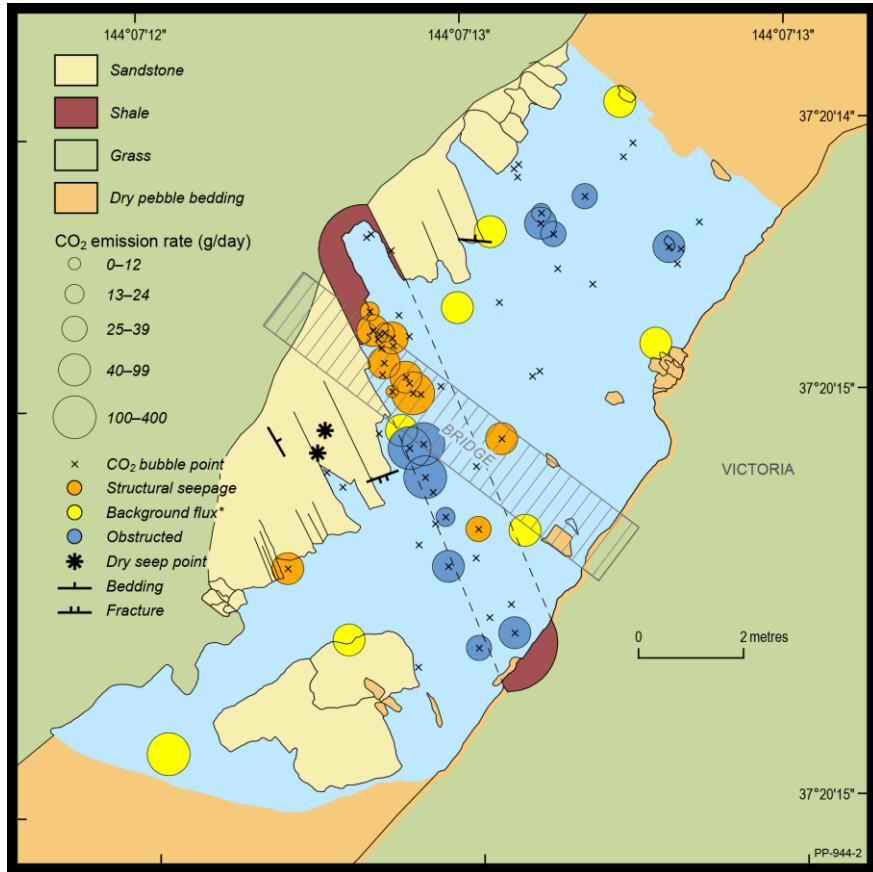
175 **Results**

176 *Field observations*

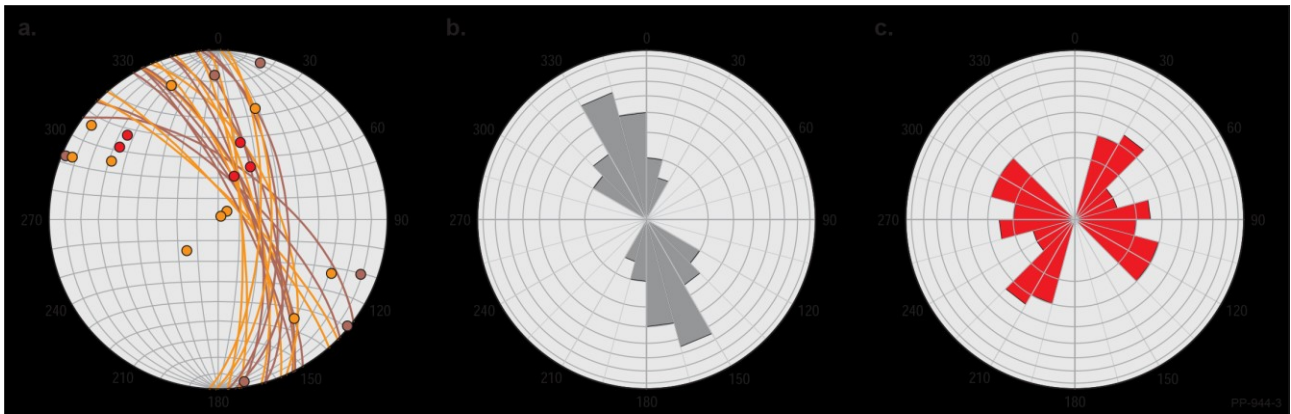
177 The low creek level in March 2017 meant that a series of isolated pools were found in the bed of
178 Sailors Creek rather than a flowing stream. CO₂ degassing characterised by numerous bubble
179 streams was observed in a single pool of water close to the footbridge near to Tipperary Mineral
180 Spring (Figure 2). The surface area of the pool was ~61.8 m² and water depth was greatest (40 cm)
181 in the centre of the creek.

182 Two units of Ordovician rock crop out in the creek bed. The majority is fine-grained buff coloured
183 massive sandstones that occur in 1 to 3 m thick beds, but a ~2.2 m thick blue-grey shale layer crops
184 out beneath the footbridge. Rock bedding is oriented NW-SE and dips 65 - 80° to the NE (Figure
185 3a,b). In contrast to the sandstone, the shale is thinly bedded (cm scale) with moderately well-
186 developed bedding and parallel foliation. The shale is fissile, and more weathered than the
187 sandstone and is less well exposed at the creek edge. The sandstone is much more cohesive, and
188 while the fracture density is lower than in the shale, the fractures are longer. Three sets of fractures
189 and joints are observed at the outcrop (Figure 3a,c). The primary fracture set trends ~NE-SW and
190 dip steeply to the SE. These vary between ~10 - 50 cm spacing, and fractures in the sandstones
191 extend through the shale. At least two exposed fractures in the sandstone show evidence of vuggy
192 quartz mineralisation. In the shale, the NE-SW fractures are closer spaced (~10 cm) but shorter;
193 often terminating before the sandstone. A second set of shallow-dipping fractures trend ~NW-SE;
194 these are mostly restricted to the sandstone unit, some are mineralised with quartz, several are

195 non-planar or are not laterally pervasive. There is no visible offset along this fracture set, thus they
196 could classify as joints. A final minor set of near vertical fractures trend E-W. These are poorly
197 developed, only centimetres in length, with large (~1 m) spacing and no clear evidence of
198 mineralisation at the outcrop.



199
200 **Figure 2:** Detailed map of the study area in Sailors Creek at Tipperary Springs Reserve showing the locations of CO₂
201 bubble streams (cross), and where measured, CO₂ seep rate depicted by the size of the halo (g/d). The colour of the
202 halo represents whether the bubble visibly emerged from a structural feature (foliation, fracture or bedding plane;
203 orange), or was not visible either because the seep point was obscured by river sediment or water depth (blue). In
204 addition, background flux was measured at sites denoted by the yellow dots. Many of the bubble streams are positioned
205 close to the lower contact between the sandstone and the shale. The principal bedding and fracture orientations are
206 shown on the map. Two locations of focussed dry seepage were observed, where CO₂ emission was detected from the
207 outcropping rock (asterisks). The river flows to the North East, but fieldwork was conducted in dry season when creek
208 fill occurred as isolated pools (though CO₂ bubbling occurred in only one pool).



209

210 **Figure 3:** Structural data from outcropping Ordovician turbidites of the Castlemaine Formation in the river bed at
 211 Tipperary Spring showing (a) Stereonet of bedding and bedding-parallel cleavage plotted as great circles, and poles to
 212 open fracture planes and poles to veins (where sandstones, orange; shales, brown; veins, red); (b) rose diagram of
 213 bedding and (c) fracture orientation, including open fractures and veins (shallow dipping fractures will be under-
 214 sampled). Structural data was analysed using Orient software (Vollmer, 2015).

215 *CO₂ seepage from submerged rock in Tipperary pool*

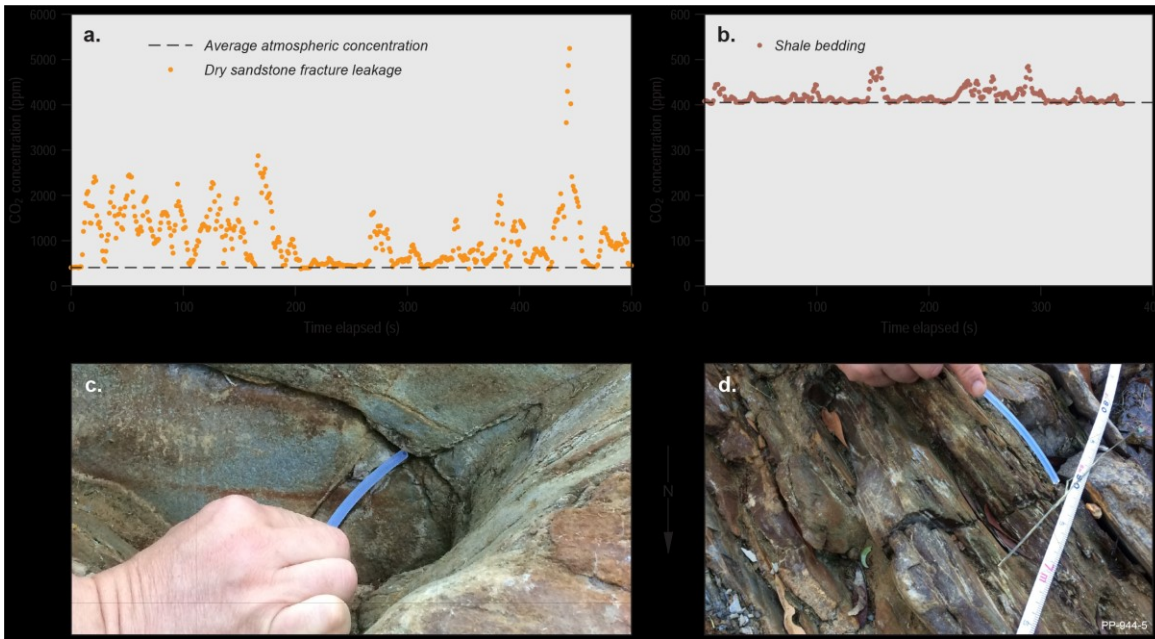
216 Figure 2 shows the locations of CO₂ bubble streams in Tipperary pool. The activity of the bubble
 217 streams varied in regards to how long they were active (bubbles emitted) and inactive (no bubbles
 218 emitted). Some were extremely intermittent, with many minutes, sometimes half an hour before
 219 another bubble exhalation, and the bubble streams short lived. Others lasted many seconds, and
 220 were comprised of a continuous exhalation of small bubbles. More persistent seeps could bubble
 221 for up to seven minutes and were only interrupted with brief pauses. In total, 60 underwater
 222 degassing points (bubble streams) were identified and mapped within Tipperary pool, and CO₂
 223 fluxes were measured at 24 (40%) of the locations.

224 75% of the bubble streams with measured fluxes were located in the shale, and preferentially
 225 towards the contact between the shale and the sandstone. CO₂ bubbles emerged along submerged
 226 foliation planes within the shale, along bedding planes of the sandstone or at the intersection
 227 between the foliation and open fractures or bedding and fractures. 46% (11/24) of the bubble
 228 streams with measured fluxes emerged from small fissures offered by dilated foliation or bedding
 229 planes, and nearly half of these occurred where open fractures or joints intersect the foliation or
 230 bedding plane. The origins of the remaining 13 bubble streams were obscured; either by sediment
 231 or because it was not possible to see to the bottom of the pool as the water was quite turbid (due
 232 to ferruginous flocculate and algae), a common feature of many of the mineral springs (Shugg and
 233 Brumley, 2003).

234 Background diffuse degassing rate was measured at eight (non-bubbling) locations across Tipperary
235 pool and ranged from 49.4 – 229 g m² d⁻¹ (mean 79.2 g m² d⁻¹). These values were relatively high
236 compared with emissions at other spring-fed pools in the Daylesford region (Roberts et al., in press),
237 and suggests that the dissolved CO₂ content of the pool water is high, but also variable across the
238 pool, but no water samples were collected to verify this. The minimum daily emission rate for the
239 pool was estimated by applying the average of the background readings across the surface area of
240 the pool and neglecting the input of bubbling points giving a value of ~4900 g d⁻¹. Degassing rates at
241 bubbling points ranged from 11.4 to 374 g d⁻¹. These values will represent combined emission of
242 CO₂ from bubbles and water surface degassing. Bubbling rates were greatest at the sandstone-shale
243 contact beneath the footbridge (figure 2). The maximum daily emission rate from the pool was
244 calculated by assuming that bubbling from the point sources was continuous and adding the sum of
245 the maximum measured bubble point emissions (2267 g d⁻¹) to the maximum background degassing
246 rate giving a value of 7170 g d⁻¹. Yearly emissions from the pool can therefore be constrained within
247 the lower and upper estimates of 1.8 – 2.6 t y⁻¹, which correspond to average flux rates across the
248 pool area of 79 - 116 g m² d⁻¹.

249 *CO₂ seepage from outcropping rocks*

250 The CO₂ sniffer detected two locations where atmospheric CO₂ concentrations were up to 6,000
251 ppm in the dry outcrops on the banks of the creek. In both cases the high CO₂ concentrations were
252 extremely localised, and occurred in jogs or intersections in uncemented, bedding-orthogonal,
253 fractures in sandstones (Figure 4a,c). Further, these concentrations were consistently high. That is,
254 returning to the same location several minutes later, similarly high concentrations from between
255 2,000 to 6,000 ppm were recorded. Consistently high CO₂ concentrations at these features suggests
256 that seepage was continuous during the survey period (several hours), and also rules out the
257 possibility that elevated CO₂ concentrations were an artefact caused by density-driven pooling of
258 CO₂ degassed from the pool at times of particularly low wind speed. Interestingly, when we poured
259 ~1L water over the seeping fracture the CO₂ concentration returned to background atmospheric
260 levels and took 14 minutes for CO₂ seepage to become re-established. Weak elevations in CO₂
261 concentration (up to 500 ppm) were detected along a bedding-orthogonal fracture in the foliated
262 shale (Figure 4b,d). However, the area of shale outcrop was less than the sandstone (in part due to
263 bedding thickness, in part due to the morphology of the outcrop) and so we cannot compare
264 instances of CO₂ detection per area of rock.



265



266

267 **Figure 4:** (a) CO₂ concentration data recorded every second by the 'CO₂ sniffer' (a LI-COR 81000A soil gas flux system)
 268 when the inflow tube was positioned (a) around a fracture intersection in a sandstone bed (orange) and (b) across shale
 269 units (red). Concentration spikes in (a) and (b) indicate where the sniffer passed over points of very localised degassing,
 270 and the concentration then varies as the tube is moved along the features, or back and forth over points of high
 271 concentration. (c) Photograph of a sandstone bedding surface intersected by two fractures. High CO₂ concentrations
 272 shown in (a) were detected at this fracture intersection and at two jogs, detailed in (e). (d) Photograph of a fracture
 273 cutting the foliated shale unit. Peaks in CO₂ concentration along this fracture were much lower, as shown in (b).
 274 Photographs (e) and (f) show the specific points of CO₂ degassing from the sandstone.

275 *Spatial distribution of seepage*

276 We use a two-point spatial correlation function (TPCF) to quantitatively investigate the alignment
 277 of mapped CO₂ bubble streams with geological structures at Tipperary. The TPCF quantifies the
 278 departure from homogeneity of a distribution of points, and the distribution of azimuths between

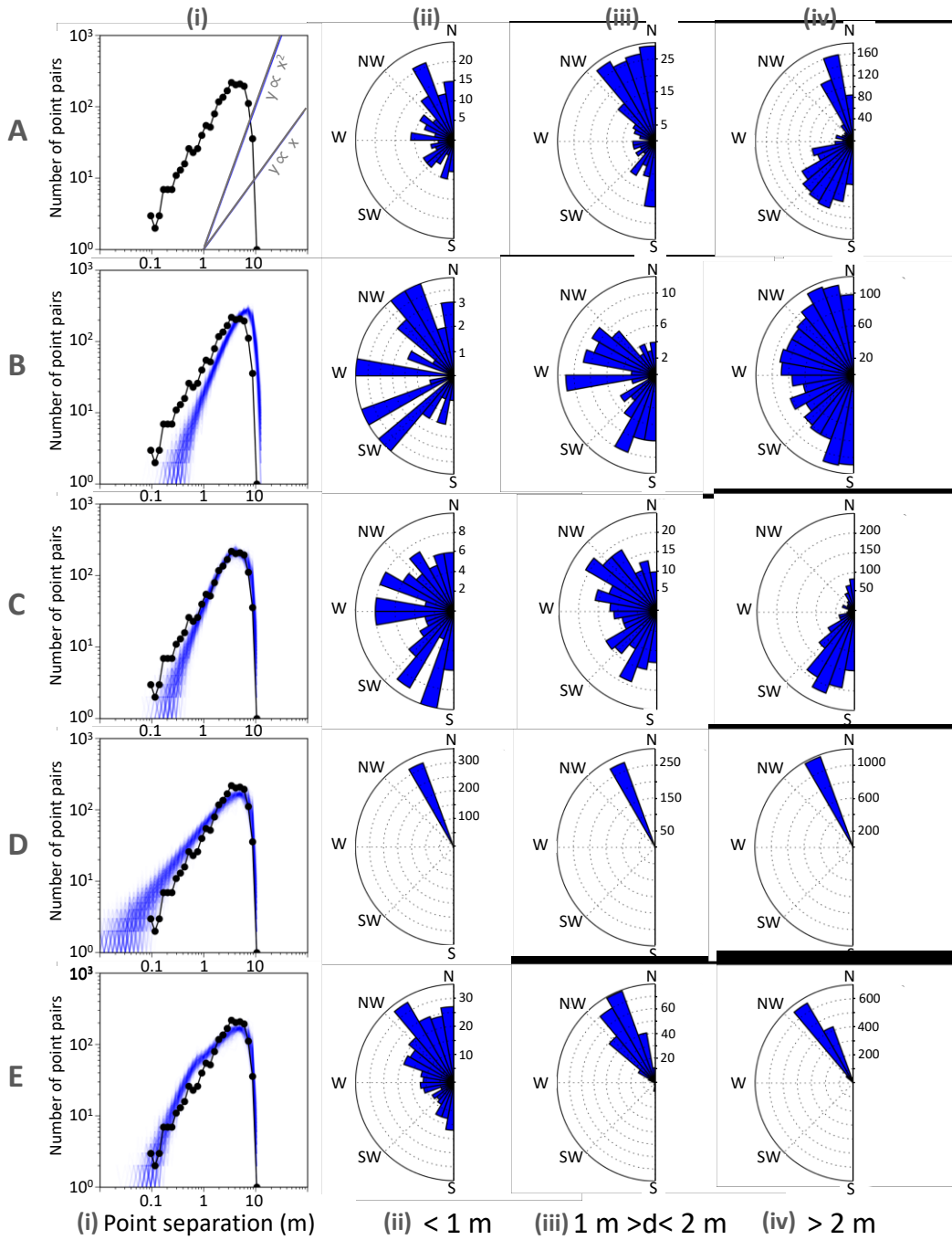
279 all point pairs can be measured to examine anisotropy in the point distribution. The correlation
280 function is expressed as the probability of finding a pair of points within incremental radius and
281 azimuth. For an ideal scenario with no finite size effects the correlation function will plot as a power
282 law, $P \propto r^\kappa$, where P is probability, r is radius, and the constant κ describes the spatial distribution of
283 points. For randomly distributed points, $\kappa = 2$. If points are clustered, $\kappa < 2$. For points that are
284 distributed on a line, $\kappa = 1$. Other arrangements, such as points distributed on multiple lines, will
285 give κ values between 1 and 2.

286 The study area is spatially limited; the pond is asymmetric and approximates a 11 x 5 m rectangle.
287 As such, synthetic data was created to act as a 'control' for comparison with the CO₂ bubble stream
288 distributions. The total numbers of measured and synthetic points are the same (60). Synthetic data
289 were generated from multiple random (Poisson) point distributions for different spatial scenarios,
290 including an 11 x 11 m exposure and an 11 x 5 m exposure with long axis orientated NNE, mimicking
291 Tipperary pool which is only 4.4 m at its narrowest point and longer in the NE-SW orientation (see
292 Figure 2). Additional synthetic data were generated for different spatial scenarios, outlined in Table
293 inset Fig 5, including Poisson distribution along a line (orientated 330° within a 10 x 5 m exposure,
294 long axis NNE), or within a given distance of a line, to explore which distribution best describes the
295 observed data.

296 TPCF results, shown in Figure 5, are presented for the bubble points and for synthetic scenarios. The
297 roll-off at distances > 4 m is a finite size (censoring) effect caused by the spatial extent of the outcrop
298 (e.g. Bonnet et al., 2001). For the synthetic data, κ is affected by the dimensions of the study area
299 (outcrop/pool); for scenario B, random points in a 10 m square, κ is close to 2 (random) whereas for
300 scenario C, κ is ~ 1.75 . Since κ values < 2 indicate clustering of point data, even for Poisson data, this
301 is a finite-size (censoring) effect caused by the spatial extent of the outcrop creating an artificial
302 alignment amongst point data. Reducing the width of the rectangle reduces the κ value, until the
303 extreme case, scenario D, where points are distributed on a line, when $\kappa = 1$. For bubble data, $\kappa =$
304 ~ 1.5 . This TPCF pattern is best modelled by scenario E, where the width of rectangle is thinner than
305 the shale outcrop.

Correlation function

Point pair azimuths



306

Point data	Description	
A	CO ₂ bubble locations at Tipperary spring	
Synthetic data	B	Points randomly distributed within 11 x 11 m square.
	C	Points randomly distributed within 11 x 5 m rectangle, long axis orientated NNE (simulating the outcrop extent).
	D	Points randomly distributed along a line, 11 m long, orientated ~NW (simulating points located directly along a fault or geological contact).

	E	Points randomly distributed within 11 x 1 m rectangle, long axis orientated ~NW (simulating points located within a bed, or around a fault or geological contact)
--	---	-------------------------------------------------------------------------------------------------------------------------------------------------------------------

307 **Figure 5:** (i) Point-distance correlation functions for observed seep pairs (black) and synthetic point simulations (blue)
308 for scenarios A to E. Polar plots show the azimuths and number of point pairs with separation distances (ii) below 1 m;
309 (iii) greater than or equal to 1m but less than 2 m; and (iv) greater than or equal to 2 m but less than 10 m. Roll-off in
310 the TPCF occurs at ~4 m separation distance due to the outcrop extent. **Table inset:** Summary of the different spatial
311 scenarios for seep point data and synthetic data.

312 Point pair azimuths at different point separation distances are shown in Figure 5 for bubble point
313 (scenario A) and synthetic (scenarios B-E) data. More point pairs are located at shorter distances in
314 the bubble data than in the synthetic data; there are over twice as many bubble point pairs within
315 less than 1 m of each other than for the synthetic data C (164:75). Since the total number of points
316 in the datasets are the same, these differences illustrate that the bubble points are more clustered
317 than in all synthetic datasets.

318 At point separation distances above 2 m the finite size effect caused by the orientation of the study
319 area clearly influences the point pair azimuths. In scenario C the rectangle is orientated NNE like the
320 Tipperary pool, whereas other synthetic scenarios are orientated NW, like the bedding at Tipperary.
321 The >2 m point pair azimuths in these synthetic scenarios clearly reflect the orientation of the
322 rectangle long axis (Fig 5iv). The effect of the orientation of Tipperary pool is evident in the bubble
323 point pair azimuths, as is the control of the NNW trending bedding/foliation 5A(iv). The control of
324 bedding/foliation on bubble pair azimuths continues to be visible at point pair distances below 2 m
325 5A(ii,iii); 38% (63 pairs) of bubbles located within <1 m of each other, and 51% of bubbles located
326 between 1 – 2 m of each other exhibit a NNW-SSE (315°–360°) orientation. In contrast, since
327 synthetic data are all randomly distributed in a given space, the dimensions of the study area are
328 not visible in the point pair azimuths at distances <2 m (except for scenario D, where point pair
329 azimuths are the same at all separation distances).

330 While bubbling points were observed in the field to be located along bedding, foliation and fracture
331 planes, the point azimuths < 2 m do not exhibit very clear spatial trends other than the bedding and
332 foliation. At Tipperary, a range of fracture orientations were measured (see Fig 3c) with dominant
333 sets trending NE-SE and NW-SE. Bubble pairs do show peaks in these orientations at < 2 m
334 separation, but it is difficult to distinguish these from noise.

335 **Discussion**

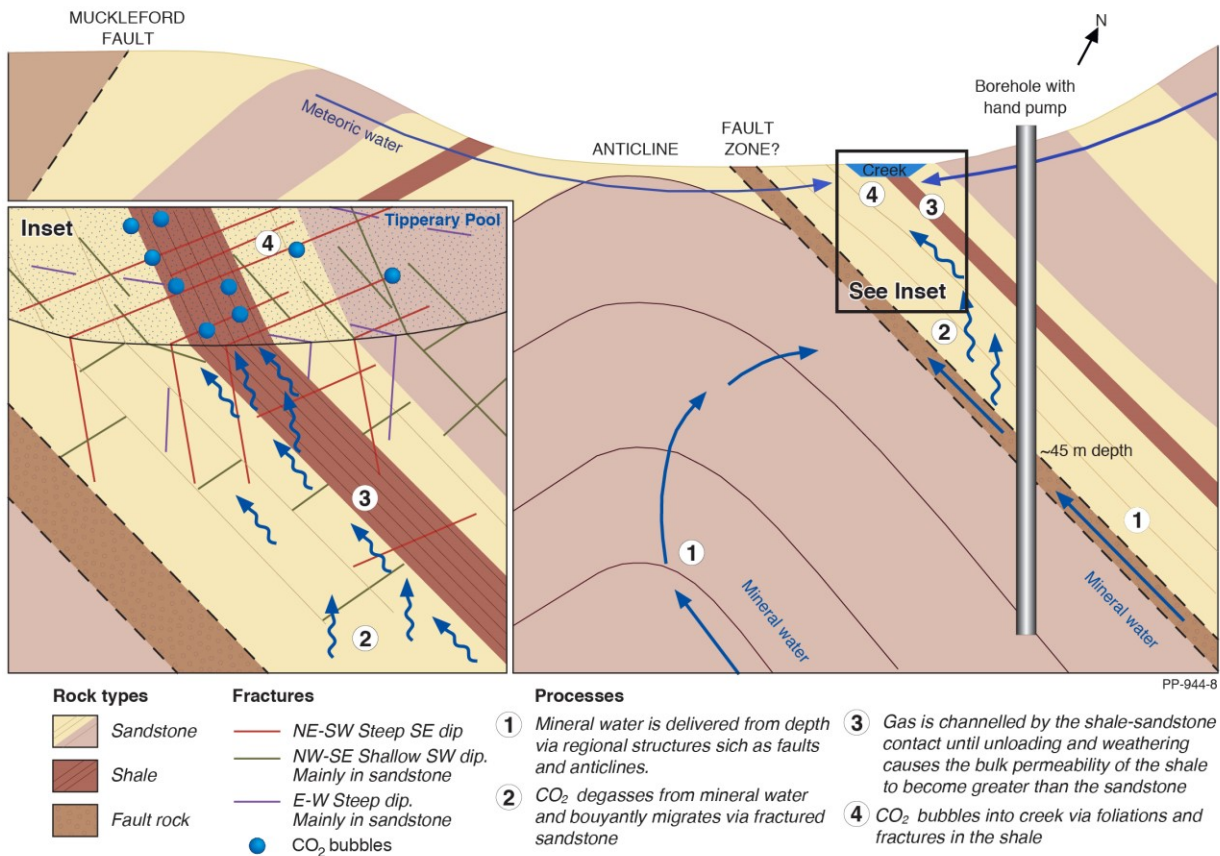
336 *The role of geological structures and CO₂ seepage at Tipperary*

337 Central Victorian mineral water springs are commonly channelled by regional thrust faults and can
338 emerge close to anticline crests (Shugg, 2009). Although obscured in the field area, the regional
339 geological map shows an inferred NNW-SSE trending anticline to the West of Sailors Creek, its
340 projected axis passing less than 20 meters from the creek. An inferred NW-SE fault runs in the same
341 orientation as the creek but is mapped as terminating before intersecting the creek (Figure 1). In
342 1912 the Daylesford Borough Engineer developed a cement-lined pit approximately 50 m SW of the
343 current location of CO₂ degassing. This pit is now in disrepair, but was built to channel the spring
344 waters, for ease of access to the mineral spring. The engineer's sketches of the area around the pit
345 record a NE-SW trending fault and a NNW-SSE trending fold, and Shugg (2004) interprets that
346 Tipperary Mineral Spring is located on the surface intersection of a thrust fault. Today, there is no
347 clear evidence of this fault at outcrop. A borehole drilled in 2001 (for the handpump) is likely to have
348 intersected this fault as indicated by the flow of gassy mineral water encountered at 45 m depth
349 (Shugg, 2004). The flow of mineral waters carrying dissolved CO₂ from depth towards the surface
350 may be guided by the geological structures such as the fault and/or the nearby anticline, similar to
351 the hypothesis of Shugg (2009). The presence of ponded water in an otherwise dry creek during the
352 dry season implies that mineral waters are seeping into the creek bed at the location of degassing.
353 However, the mineral waters probably degas CO₂ during their ascent to surface; we observed dry
354 seepage from outcropping rocks, while at nearby springs down-hole camera surveys found bubbles
355 starting to form around 20–30 m below the water table (Shugg 2009). When two-phase flow
356 establishes, the CO₂ may migrate to surface via different pathways to its 'parent' water, depending
357 on the hydraulic properties of the available flow pathways and water table depth. There is no
358 appreciable thermal anomaly between the mineral waters and the surrounding groundwater
359 (Weaver et al., 2006), so they are not ascending due to thermal buoyancy drive. Instead they may
360 be migrating towards the surface due to a combination of hydraulic head and the fluid flow
361 pathways offered by nearby structures, enhanced by buoyancy from gas lift due to CO₂ ebullition as
362 the waters depressurise during ascent.

363 CO₂ seepage at Tipperary spring concentrates near the western sandstone-shale contact. Some 81%
364 of total measured bubble stream emissions emerge from the shale dominated features in the river
365 bed and we detected extremely localised dry seepage from open fractures within outcropping
366 sandstone and shale. The bedding and foliation orientation of rocks exposed in Sailors Creek follows
367 the regional trend from NNW-SSE Devonian compression. Our spatial statistical analyses find that

368 bubble point data exhibit this NNW-SSE (150-170°) trend at all point separation distances. Bubble
369 points located within <2 m of each other show other preferred alignments (NE-SW and SE-NW, NNE-
370 SSW, ENE-WSW) but these trends are weak compared to the NNW orientations. Seepage mostly
371 occurred in a narrow region, ~1 m width. In the field, we noted that bubble locations appeared to
372 be primarily controlled by bedding and foliation planes, but also by fractures and joints across both
373 the sandstone and shale members. Thus, while regional structures may govern mineral water and
374 CO₂ flow (Shugg, 2009), it seems that primary features (the sandstone-shale contact) may control
375 fluid flow in the deep and shallow subsurface, and at very shallow depths the small secondary
376 structures (fractures, foliation) offer pathways to surface.

377 What is unusual at Tipperary is that gas primarily discharges from shales. Mudrocks and shales
378 typically have low permeabilities, and high capillary entry pressures for two-phase flow, which
379 makes them good seals for conventional hydrocarbon traps. At other sites around Daylesford, such
380 as Sutton Spring, mineral water and gas discharges from the joints and fracture faces in sandstone
381 beds (Shugg, 2009). These sandstones form the regional aquifer. Within these sandstone units
382 intergranular porosity is limited to certain horizons. Therefore, groundwater flow is predominantly
383 hosted by fractures and joints. Observations from exposed bedrock at Tipperary suggest that bulk
384 rock permeability is most likely offered by the primary fracture set (NE-SW trend) together with the
385 bedding. However, at Tipperary, our observations, corroborated by spatial statistical analyses, find
386 that CO₂ bubbles preferentially emerge from foliation and fracture intersections in the shale. This
387 indicates that in the shallow subsurface the high density of subvertical foliation and bedding-
388 orthogonal fractures in the shale must be more transmissive than bedding and fracture planes in
389 the sandstone. At outcrop, the fractured, folded and uplifted shales of the Ordovician succession
390 clearly are not sealing. This could be due to unloading and weathering, and so these pathways have
391 opened only close to the surface. Conversely, the bulk permeability of the shale units may be greater
392 than the sandstone for these units. Figure 6 schematically summarises the proposed mechanism for
393 CO₂ delivery to the creek bed at Tipperary.



394

395 **Figure 6:** Schematic 2D cross section (not to scale) of proposed model for CO₂ and mineral water flow pathways that
 396 give rise to Tipperary Mineral Spring and CO₂ seep. Inset: schematic 2.5D closeup of Tipperary Pool. While the shale may
 397 not be transmissive to fluids at depths where foliation and fractures are closed by overburden pressure, we propose
 398 that in the shallow subsurface unloading and weathering opens bedding, foliation and fractures enabling the shale to
 399 transmit fluids more readily than the fractured sandstone aquifer rocks. This causes the majority of CO₂ to be emitted
 400 via well-connected flow pathways in the shale unit in Tipperary Pool, and manifests as numerous and intermittent low
 401 flux bubble streams. CO₂ that is emitted straight to atmosphere ('dry seepage') is not intermittent. This implies that the
 402 turning 'on' and 'off' of bubble streams SW may result from capillary flow processes in the very shallow subsurface.

403 Other seeps worldwide emerge from clays. For example, in the Cheb Basin, CO₂ degassing close to
 404 a fault zone in clay dominated rocks occurs as highly localised emissions from fine fractures,
 405 facilitated by "micro-channels" in the clays which originated from shear (Bankwitz et al., 2003).
 406 Where low permeability rocks outcrop in Italy, CO₂ degassing occurs as vent like emissions rather
 407 than as springs or spring associated emissions, which more commonly occur from high permeability
 408 rocks (Roberts et al., 2014). However, at Tipperary, what is surprising is that CO₂ preferentially
 409 emerges from the shales rather than the sandstones.

410 That said, CO₂ seepage is not confined to the shale. Seepage occurs from sandstones submerged in
 411 Tipperary pool, and the CO₂ sniffer detected high CO₂ emissions from isolated points in the

412 outcropping sandstone. Therefore there are gas flow pathways in the sandstone, but there are
413 fewer pathways in the sandstone than in the shales (where gas emission is greater), and these
414 pathways are extremely localised; occurring at jogs and intersections along low-dip bedding-
415 orthogonal fractures, where they intersected the bedding plane (Figure 5e).

416 Interestingly, the sniffer results indicate that it is likely that dry CO₂ seepage is greater from the
417 outcropping sandstone than from outcropping shale. This is in contrast to CO₂ fluxes measured in
418 Tipperary pool where more numerous and distributed bubble streams occur in the shale, and 75%
419 of the total CO₂ flux via bubbles from Tipperary Pool is occurring from the shales. It is possible that
420 this is a sampling artefact; the seep area is limited, the shale bed is thinner than the sandstones,
421 and the area of outcrop is much smaller for the shale because it has preferentially eroded on the
422 creek banks. If this is a real signal, there could be several explanations for the contrasting behaviour
423 of the seeps through water and into air. Firstly, the rate of CO₂ seepage through the two lithologies
424 could be the same but is occurring via distributed pathways (lots of small fractures and bedding
425 partings) in the shale, with fewer localised high flux fracture-bedding intersections in the sandstone.
426 As the shale was more foliated and thinly bedded, there were many more bedding parallel features
427 to permit flow and so facilitate distributed seepage than in the massive bedded sandstone.
428 Secondly, the outcrop style varies between the two lithologies: the sandstone stands proud of the
429 surface and some individual bedding planes are exposed, whereas the shale is more eroded and the
430 bedding is only viewed end-on. This means that the fractures that are low-dip (which are the ones
431 that host the high dry seepage from the sandstone) are exposed in the sandstone, but are unlikely
432 to be exposed in the shale at this site. Thirdly, flow pathways in the sandstone might be more likely
433 to become obstructed by river sediments than the smaller aperture features in the shale. Regardless
434 of the reason, our observations suggest that flow pathways in the very shallowest subsurface, and
435 therefore how CO₂ seeps present, are highly sensitive to local conditions.

436 *CO₂ flux at Tipperary*

437 Estimating total CO₂ flux at Tipperary Spring is challenging given the intermittency of the CO₂ bubble
438 streams. Bubbling, and therefore CO₂ flux, was not continuous in the pool. The flux of CO₂ from
439 depth is probably continuous, but the bubbles are intermittent either due to high connectivity of
440 the flow pathways (with flow paths turning 'on' and 'off') and/or due to water saturation of the flow
441 pathways; CO₂ gas pressure must build enough to overcome capillary flow pressure, and the
442 pressure of the water in the fracture. Such temporal and spatial variability has been observed at

443 other CO₂ seeps including Laacher See (Germany - CO₂ bubbling is observed from the floor of a crater
444 lake), Panarea (Italy - submarine geothermal region) and at the QICS project (Scotland - simulated
445 CO₂ leak to the marine environment) Blackford et al. (2015) and Carammana pers. comm (2017). At
446 a larger spatial scale, temporal and spatial variability in CO₂ emission has been observed at the Little
447 Grand and Salt Wash faults in Utah over tens of thousands of years (Burnside et al., 2013). As such,
448 intermittency of gas bubbling could be a universal phenomenon associated with gas flux into
449 heterogeneous water-saturated media. This phenomenon is not restricted to CO₂. For example, the
450 authors have observed intermittent bubbling of gases (predominantly nitrogen, but including CO₂,
451 CH₄ and other short chain hydrocarbons) into creek beds in Northumberland (UK), and presumed to
452 source from abandoned underground coal mines, which are common in this region.

453 Dynamic seepage has implications for strategies for sampling of natural gases, and also for
454 estimating gas fluxes or total emissions. At Tipperary, the minimum total flux can be estimated from
455 background diffuse degassing (79.2 g m⁻²d⁻¹ or 4 kg y⁻¹), which does not include the contribution of
456 individual bubbling seeps. Maximum flux can be estimated by assuming all measured bubble
457 streams are active simultaneously, which equates to 116 g m⁻²d⁻¹. However, since few bubble
458 streams were active at the same time, this is an overestimate. In addition, our estimates do not
459 consider dry CO₂ seepage from rocks by the pool, CO₂ dissolution (if the pool is not already
460 saturated), or seasonal changes in the CO₂ emission.

461 Previous studies at natural CO₂ seeps find a range of CO₂ fluxes over several orders of magnitude,
462 which poses challenges for the selection of appropriate monitoring devices and approaches. The
463 rate of degassing depends on factors including soil and rock permeability, hydrogeological regime,
464 and nature of the CO₂ source (Annunziatellis et al., 2008, Kirk et al., 2011). Fluxes at dry seeps such
465 as mofettes can be very high e.g. 9000 g m⁻²d⁻¹ at Florina (Greece) and 125,000 g m⁻² d⁻¹ in the Cheb
466 Basin (Germany/Czech Republic) (Nickschick et al., 2015). But mofette systems are different from
467 CO₂ degassing at mineral springs. Recent work at travertine bearing fault systems report fluxes that
468 are more similar to Tipperary; maximum CO₂ fluxes were 191 g m⁻²d⁻¹ at the Bongwana Fault (South
469 Africa) (Bond et al., 2017) and calculated from travertine mass balance to be 1,472 ± 677 and 18.8
470 ± 8.7 g m⁻²d⁻¹ at two sites in Utah (USA) (Burnside et al., 2013).

471 Natural non-volcanic seeps are the most appropriate analogues for seeps that might potentially
472 develop above engineered carbon stores, if injected CO₂ seeps to the surface by natural CO₂
473 pathways. However there are limitations to their comparability. Storage sites will be selected for

474 specific sealing characteristics. In contrast, surface seepage at natural CO₂ seeps occur *because* the
475 geology is not ideal for long term CO₂ trapping; the geology around Daylesford is composed of highly
476 heterogeneous and tectonised sediments crossed by faults. Faulted reservoirs with heterogeneous
477 or poorly permeable overburdens will probably not be selected for long term geological storage. In
478 addition, natural CO₂ seeps will be migrating by natural fluid pathways whereas the greatest risks of
479 CO₂ leakage from engineered CO₂ stores are man-made pathways, such as improperly sealed
480 boreholes (IPCC, 2005) or geomechanical effects from the pressure response to CO₂ injection
481 (Verdon et al., 2013). That said, natural CO₂ seeps may still be comparable to leakage through the
482 overburden, independent of the leakage pathways from the reservoir, and seepage through clay
483 formations, can serve analogues of CO₂ migration through cap rocks.

484 *Implications for CCS*

485 It is important to assure regulatory bodies and the public of CO₂ storage integrity. This includes
486 demonstrating capability to (i) select storage sites that will successfully retain CO₂ in the subsurface,
487 and (ii) identify potential CO₂ leakage and (iii) quantify any leaked CO₂.

488 In the case of CO₂ migration from onshore engineered storage sites, if the leaked CO₂ migrates to
489 the near surface it could dissolve into groundwaters (and perhaps emerge as a dissolved constituent
490 of groundwaters at natural springs), seep to atmosphere as a dry gas, or seep into water bodies such
491 as lakes or rivers. Where migrating CO₂ dissolves into groundwaters, the groundwater flow systems
492 will then govern its flow path, and only at shallow depth will decreasing pressures cause gas
493 ebullition and facilitate the ascent of a separate gas phase. Indeed, studies of onshore natural
494 analogues and field sites find that CO₂ seeps are more likely to emerge in topographic low points
495 where there may be rivers or lakes, though there are examples of seeps that buck this trend (e.g. if
496 flow is fault controlled) (Roberts et al., 2014).

497 In this work, we examine the surface expression of CO₂ seepage originating from transport of CO₂-
498 rich regional groundwaters. We find that, while regional features may govern CO₂ delivery, in the
499 shallow subsurface CO₂ pathways are localised to small scale geological features, and that fluxes are
500 intermittent and consequently difficult to quantify due to the intermittency of bubbling pathways.

501 To date, most research has focussed on predicting the large-scale geological features that may
502 enable CO₂ to migrate from the storage reservoir such as large faults, boreholes or gas chimneys
503 (IEAGHG, 2017). Such macroscale (seismically resolvable) features are likely to be known about at
504 the site characterisation phase of a project. However, shallow crustal processes change the rock

505 properties that affect CO₂ spread and delivery to surface. Different, smaller scale geological
506 features, that are not likely to be seismically resolvable, may become important controls on CO₂
507 flow in the shallow subsurface. At Tipperary, CO₂ seep distribution is controlled by microscale
508 features such as foliation and bedding planes, joints and fractures in outcropping rock, probably
509 dilated by uplift and weathering, which leads to degassing from a shale formation that is typically
510 sealing. These observations support previous research investigating the role of topography and
511 lithology in CO₂ seep location and characteristics (Roberts et al., 2014), and has important
512 consequences for the design of CCS monitoring approaches. Surface monitoring programmes must
513 focus on more than the processes and pathways governing leakage at depth; they must also
514 consider how the CO₂ fluids leaked by natural or man-made pathways might disperse in the near
515 surface and be expressed at the surface. These shallow processes will inform the design of the right
516 monitoring tools and monitoring locations.

517 Our work thus provides insight into the scale of which geological features control CO₂ flow and the
518 spatial and temporal variability of CO₂ leakage. Essentially, site characterisation during site selection
519 and monitoring design must assess the geology and hydrogeology at a range of spatial scales.
520 Surface processes, often overlooked, will govern the style and location of leakage, and so should
521 inform the design of appropriate monitoring strategies.

522 **Conclusions**

523 We have studied the location and characteristics of CO₂ emission at Tipperary natural CO₂ seep in
524 Daylesford, Victoria (Australia) as an analogue for leakage from engineered CO₂ stores. Seepage
525 largely occurs as bubble streams in a pool in Sailors Creek, close to the Tipperary mineral springs
526 which have high dissolved CO₂-content. We also observed CO₂ degassing from subaerial rock
527 outcrop. Observation and spatial statistical analyses find that at a meso-scale (multiple meters) the
528 location of CO₂ bubble streams are controlled by the sandstone-shale geological contact. At a
529 smaller (meter to centimetre) scale, gas emission is controlled by structural features, primarily
530 fractures intersecting the foliation or bedding planes. The intermittency of the bubble streams, and
531 their distribution, makes CO₂ flux challenging to quantify. Unusually, CO₂ emission is greatest from
532 the shale, rather than the sandstone that forms the regional aquifer. Surface processes are likely to
533 be affecting rock transmissivity, which governs CO₂ flow at the near surface. Our work has important
534 implications for characterising and monitoring of CO₂ stores: microscale features and near surface
535 processes can have significant effect on CO₂ leak locations and rates. Flow pathways through the

536 very shallowest part of the subsurface are highly dependent on local conditions, and may produce
537 the highest flux in counter-intuitive locations (e.g. hosted by the 'low permeability' shales at
538 Tipperary). Understanding of shallow crustal processes and specific site conditions are essential to
539 inform the design of effective surface monitoring tools and approaches. Secondly, should leakage
540 from the storage reservoir occur, the surface leak identification and quantitation approaches must
541 be extended to consider intermittent or variable CO₂ emission rates.

542 **Acknowledgements**

543 We are grateful for contributions, discussions, and assistance from Jade Anderson, Ivan Schroder
544 and Tim Evans (Geoscience Australia), Giorgio Caramanna (GeoAqua Consulting), Anthony Handley
545 (Parks Victoria), and Andy Shugg. We thank Bart Thomas, Ryan Ruddick and Auscope for providing
546 RTK equipment and training and Suman George (University of Western Australia/National
547 Geosequestration Laboratory) for providing the Li-COR 81000A soil gas flux system. Many thanks to
548 David Arnold (Geoscience Australia) for his help preparing the illustrations in this paper. We also
549 thank Sabina Bigi and her team at Sapienza Università di Roma for providing information on the
550 composition of gases observed bubbling into streams in Northumberland in 2017.

551 The authors would like to acknowledge the financial support of the UK CCS Research Centre
552 (www.ukccsrc.ac.uk) in carrying out this work (grant number UKCCSRC-C1-31). The UKCCSRC is
553 funded by the EPSRC (EP/K000446/1, EP/P026214/1) as part of the RCUK Energy Programme. We
554 also thank the UKCCSRC, University of Strathclyde, CSIRO and Geoscience Australia for supporting
555 this work through Roberts' International Research Collaboration Fund. Our collaborative fieldwork
556 in Northumberland with Sapienza Università di Roma was supported by the University of Strathclyde
557 and the EU-funded ENOS project (H2020-EU.3.3.2.3; grant no. 653718).

558 **Annex A: Accumulator chamber factor for CO₂ flux measurements**

559 To convert the rate of change in CO₂ concentration measured in the accumulation change (e.g. in
560 ppm/s) to a flux (mole/m²/day), the rate needs to be multiplied by a correction factor which
561 considers the volume of the chamber, temperature and pressure:

$$562 \quad K = \frac{86400 \cdot P}{10^6 \cdot R \cdot T_k} \cdot \frac{V}{A}$$

563 where

- 564 • P is the barometric pressure expressed in mBar

- 565 • R is the gas constant 0.0831451 bar L K⁻¹ mol⁻¹
- 566 • T_k is the air temperature expressed in degrees Kelvin
- 567 • V is the chamber net volume in cubic meters (less the portion of the chamber submerged to
- 568 create a seal on the water surface)
- 569 • A is the chamber inlet area in square meters

570

571 **Data Availability Statement**

572 All data (precise bubble locations and distributions, fluxes, and whether bubbling occurred at a
573 fracture or foliation/bedding at Tipperary pool), are available from the UKCCSRC Data and
574 Information Archive, under the DOI: (to be added).

575

576 **References**

577 Annunziatellis, A., Beaubien, S. E., Bigi, S., Ciotoli, G., Coltella, M., and Lombardi, S., (2008) Gas
578 migration along fault systems and through the vadose zone in the Latera caldera (central Italy):
579 Implications for CO₂ geological storage: International Journal of Greenhouse Gas Control, v. 2, no.
580 3, p. 353-372.

581 Bankwitz, P., Schneider, G., Kämpf, H., and Bankwitz, E. (2003) Structural characteristics of
582 epicentral areas in Central Europe: study case Cheb Basin (Czech Republic): Journal of Geodynamics,
583 v. 35, no. 1, p. 5-32.

584 Blackford, J., Bull, J. M., Cevatoglu, M., Connelly, D., Hauton, C., James, R. H., Lichtschlag, A., Stahl,
585 H., Widdicombe, S. & Wright, I. C. (2015). Marine Baseline and Monitoring Strategies For Carbon
586 Dioxide Capture And Storage (CCS). International Journal of Greenhouse Gas Control, 38, 221-229.

587 Bond, C.E., Kremer, Y., Johnson, G., Hicks, N., Lister, R., Jones, D.G., Haszeldine, R.S., Saunders, I.,
588 Gilfillan, S.M.V., Shipton, Z.K., Pearce, J. (2017). The physical characteristics of a CO₂ seeping fault:
589 The implications of fracture permeability for carbon capture and storage integrity. Int. J. Greenh.
590 Gas Control 61, 49–60. doi:10.1016/j.ijggc.2017.01.015

591 Bond, C.E., Wightman, R., Ringrose, P.S. (2013) The influence of fracture anisotropy on CO₂ flow.
592 Geophys. Res. Lett. 40, 1284–1289. doi:10.1002/grl.50313

593 Bonnet, E., Bour, O., Odling, N. E., Davy, P., Main, I., Cowie, P., and Berkowitz, B. (2001) Scaling of
594 fracture systems in geological media. *Rev. Geophys.* 39 (3), 347-383. doi: 10.1029/1999RG000074

595 Burnside, N. M., Shipton, Z. K., Dockrill, B., and Ellam, R. M. (2013) Man-made versus natural CO₂
596 leakage: A 400 k.y. history of an analogue for engineered geological storage of CO₂. *Geol.* 41 (4),
597 471-474. doi: 10.1130/G33738.1

598 Cartwright, I., Weaver, T., Tweed, S., Ahearne, D. (2002). Stable isotope geochemistry of cold CO₂-
599 bearing mineral spring waters, Daylesford, Victoria, Australia: sources of gas and water and links
600 with waning volcanism. *Chem. Geol.* 185 (1),71-89. doi 10.1016/S0009-2541(01)00397-7

601 Cartwright, I., Weaver, T., Tweed, S., Ahearne, D., (2000) O, H, C isotope geochemistry of carbonated
602 mineral springs in central Victoria, Australia: sources of gas and water–rock interaction during dying
603 basaltic volcanism. *J. Geochem. Expl.* 69-70, 257–261. doi:10.1016/s0375-6742(00)00059-5

604 Carpenter, M., Kvien, K. & Aarnes, J. (2011) The CO₂QUALSTORE guideline for selection,
605 characterisation and qualification of sites and projects for geological storage of CO₂. *Int. J. Greenh.*
606 *Gas Control* 5 (4), 942-951. doi: 10.1016/j.ijggc.2010.12.005

607 Chiodini, G., Frondini, F., Cardellini, C., Granieri, D., Marini, L., Ventura, G. (2001) CO₂ degassing and
608 energy release at Solfatara volcano, Campi Flegrei, Italy. *J. Geophys. Res.* 106, 16213–16221.
609 doi:10.1029/2001jb000246

610 Cox, S.F., Etheridge, M.A., Cas, R. (1991a) Deformational style of the Castlemaine area, Bendigo-
611 Ballarat Zone: Implications for evolution of crustal structure in central Victoria. *Aust. J. Earth Sci.* 38,
612 151–170. doi:10.1080/08120099108727963

613 Cox, S.F., Wall, V.J., Etheridge, M.A., Potter, T.F. (1991b) Deformational and metamorphic processes
614 in the formation of mesothermal vein-hosted gold deposits—examples from the Lachlan Fold Belt
615 in central Victoria, Australia. *Ore Geol. Rev.* 6, 391–423.

616 Dixon, T., McCoy, S.T., Havercroft, I. (2015). Legal and Regulatory Developments on CCS. *Int. J.*
617 *Greenh. Gas Control* 40, 431–448. doi:10.1016/j.ijggc.2015.05.024

618 Dockrill, B., and Shipton, Z. K. (2010) Structural controls on leakage from a natural CO₂ geologic
619 storage site: Central Utah, U.S.A. *J. Struct. Geol.* 32 (11), 1768-1782. doi:10.1016/j.jsg.2010.01.007

620 Faulkner, D. R., Jackson, C. A. L., Lunn, R. J., Schlische, R. W., Shipton, Z. K., Wibberley, C. A. J., and
621 Withjack, M. O. (2010) A review of recent developments concerning the structure, mechanics and

622 fluid flow properties of fault zones: *J. Struct. Geol.* 32 (11), 1557-1575. doi:
623 10.1016/j.jsg.2010.06.009

624 Feitz, A. J., Leamon, G., Jenkins, C., Jones, D. G., Moreira, A., Bressan, L., Melo, C., Dobeck, L. M.,
625 Repasky, K., and Spangler, L. H. (2014) Looking for leakage or monitoring for public assurance?
626 *Energy Procedia* 63, 3881-3890. doi: 10.1016/j.egypro.2014.11.418

627 Gill, E.D. (1964) Rocks Contiguous with the Basaltic Cuirass of Western Victoria. *Proc. R. Soc. Vic.* 77,
628 331–355.

629 Gray, D.R., Willman, C.E. (1991) Deformation in the Ballarat Slate Belt, central Victoria, and
630 implications for the crustal structure across southeast Australia. *Aust. J. Earth Sci.* 38, 171–201.
631 doi:10.1080/08120099108727964

632 Gray, D.R., Wilson, C.J.L., Barton, T. J. (1991) Intracrustal detachments and implications for crustal
633 evolution within the Lachlan fold belt, southeastern Australia. *Geol.* 19 (6): 574–577. doi:
634 [https://doi.org/10.1130/0091-7613\(1991\)019<0574:IDAIFC>2.3.CO;2](https://doi.org/10.1130/0091-7613(1991)019<0574:IDAIFC>2.3.CO;2)

635 Haszeldine, R.S. (2009) Carbon capture and storage: how green can black be? *Science* 325, 1647–
636 1652. doi:10.1126/science.1172246

637 Hippler, S. J., Deformation microstructures and diagenesis in sandstone adjacent to an extensional
638 fault: Implications for the flow and entrapment of hydrocarbons, *AAPG Bull.*, 77, 625–637 (1993)

639 Holloway, S., Pearce, J. M., Hards, V. L., Ohsumi, T., and Gale, J. (2007) Natural emissions of CO₂
640 from the geosphere and their bearing on the geological storage of carbon dioxide: *Energy*, v. 32, no.
641 7, p. 1194-1201. doi: 10.1016/j.energy.2006.09.001

642 IEAGHG (2017) CO₂ Migration in The Overburden. IEAGHG Technical Reports. IEA Greenhouse Gas
643 R&D Programme

644 IPCC (2005) IPCC Special Report on Carbon Dioxide Capture and Storage. Prepared by Working
645 Group III of the Intergovernmental Panel on Climate Change.

646 Jenkins, C., Chadwick, A., and Hovorka, S. D. (2015) The state of the art in monitoring and
647 verification—Ten years on. *Int. J. Greenh. Gas Control*, v. 40, p. 312-349. doi:
648 10.1016/j.ijggc.2015.05.009

649 Karolytè, R., Serno, S., Johnson, G., Gilfillan, S.M.V. (2017) The influence of oxygen isotope exchange
650 between CO₂ and H₂O in natural CO₂-rich spring waters: Implications for geothermometry. *App.*
651 *Geochem.* 84, 173–186. doi:10.1016/j.apgeochem.2017.06.012

652 Kirk, K. (2011) Natural CO₂ flux literature review for the QICS project (No. CR/11/005). British
653 Geological Survey Commissioned Report.

654 Laing, A.C.M. (1977) Daylesford – Hepburn Springs mineral water investigation. Dept. of Minerals
655 and Energy and the Geological Survey of Victoria, Melbourne.

656 Lawrence, C.R. (1969) Hydrogeology of the Daylesford district with special reference to the mineral
657 springs 1–40. Dept. of Mines, Geological Survey, Melbourne.

658 Maddicks, H.T., Butler, K.H. (1981) 100 Years of Daylesford Gold Mining History. Daylesford
659 Historical Society, Victoria.

660 Magara, K. (1993) Pressure sealing: An important agent for hydrocarbon entrapment. *J. Pet. Sci. Eng.*
661 9, 67–80. doi:10.1016/0920-4105(93)90029-E

662 McCay, A. T., Shipton, Z. K., Lunn, R. J., and Gale, J.F. , 2018, Mini thief zones: Sub-centimeter
663 sedimentary features enhance fracture connectivity in shales: *Bulletin of the American Association*
664 *of Petroleum Geologists*. doi:10.1306/0918181610617114

665 Mcdougall, I., Allsop, H.L., Chamalaun, F.H. (1966) Isotopic Dating of the Newer volcanics of Victoria,
666 Australia, and Geomagnetic Polarity Epochs. *J. Geophys. Res.* 71, 6107–6118. doi:
667 10.1029/JZ071i024p06107

668 Miocic, J.M., Gilfillan, S.M.V., Roberts, J.J., Edlmann, K., McDermott, C.I., Haszeldine, R.S. (2016)
669 Controls on CO₂ storage security in natural reservoirs and implications for CO₂ storage site
670 selection. *Int. J. Greenh. Gas Control* 51, 118–125. doi:10.1016/j.ijggc.2016.05.019

671 Nickschick, T., Kämpf, H., Flechsig, C., Mrlina, J. & Heinicke, J. (2015) CO₂ degassing in the Hartoušov
672 Mofette Area, Western Eger Rift, imaged by CO₂ Mapping and Geoelectrical and Gravity Surveys.
673 *International Journal Of Earth Sciences*, 104, 2107-2129.

674 OECD/IEA (2015) Carbon Capture and Storage: The solution for deep emissions reductions. IEA
675 Publishing.

676 Oldenburg, C. M., and Lewicki, J. L. (2006) On leakage and seepage of CO₂ from geologic storage
677 sites into surface water. *Environ. Geol.* 50 (5), 691-705. doi: 10.1007/s00254-006-0242-0

678 Osborne, C., Bibby, L., Willman, C., Maher, S., Hollis, J. (2002) Daylesford 1:50 000 geological map.
679 Geological Survey of Victoria.

680 Pearce, J., Czernichowski-Lauriol, I. (2004) A review of natural CO₂ accumulations in Europe as
681 analogues for geological sequestration. *Geol. Soc. London Spec. Pub.* 233, 29-41 doi:
682 10.1144/GSL.SP.2004.233.01.04

683 Richards, J.R., Singleton, O.P. (1981) Palaeozoic Victoria, Australia: Igneous rocks, ages and their
684 interpretation. *J. Geol. Soc. Aust.* 28, 395–421. doi:10.1080/00167618108729178

685 Rinaldi, A.P., Rutqvist, J. (2013) Modeling of deep fracture zone opening and transient ground
686 surface uplift at KB-502 CO₂ injection well, In Salah, Algeria. *Int. J. Greenh. Gas Control* 12, 155–167.
687 doi:10.1016/j.ijggc.2012.10.017

688 Roberts, J. J., Feitz, A. J., Leplastrier, A., Anderson, J. & Schroder, I. (in press) Quantifying CO₂ leak
689 rates in aquatic environments. SSRN: GHGT-14 Proceedings.

690 Roberts, J. J., and Stalker, L. (2017) What have We Learned about CO₂ Leakage from Field Injection
691 Tests?: *Energy Procedia*, v. 114, no. Supplement C, p. 5711-5731.

692 Roberts, J.J., Wilkinson, M., Naylor, M., Shipton, Z.K., Wood, R.A., Haszeldine, R.S. (2017a) Natural
693 CO₂ sites in Italy show the importance of overburden geopressure, fractures and faults for CO₂
694 storage performance and risk management. *Geol. Soc. London Spec. Pub.* 458, 181–211.
695 doi:10.1144/SP458.14

696 Roberts, J. J., Gilfillan, S. M. V., Stalker, L., and Naylor, M. (2017b) Geochemical tracers for
697 monitoring offshore CO₂ store. *Int. J. Greenh. Gas Control* 65, 218-234.
698 doi:10.1016/j.ijggc.2017.07.021

699 Roberts, J.J., Wood, R.A., Wilkinson, M., Haszeldine, S. (2014) Surface controls on the characteristics
700 of natural CO₂ seeps: implications for engineered CO₂ stores. *Geofluids* 15, 453–463.
701 doi:10.1111/gfl.12121

702 Schaffer, M., Maier, F., Licha, T., Sauter, M. (2013) A new generation of tracers for the
703 characterization of interfacial areas during supercritical carbon dioxide injections into deep saline
704 aquifers: Kinetic interface-sensitive tracers (KIS tracer). *Int. J. Greenh. Gas Control* 14, 200–208.
705 doi:10.1016/j.ijggc.2013.01.020

706 Shugg, A. (2009) Hepburn Spa: cold carbonated mineral waters of Central Victoria, South Eastern
707 Australia. *Environ. Geol.* 58, 1663–1673. doi:10.1007/s00254-008-1610-8

708 Shugg, A. (2004) Sustainable Management of the Central Victorian Mineral Waters. PhD, RMIT
709 University, Melbourne.

710 Shugg, A. (1996) Mineral and Spring Water Resource Protection Discussion Paper. Department of
711 Natural Resources and Environment, Melbourne.

712 Shugg, A., Brumley, J.C. (2003) Environmental, hydrogeological and conflict as elements determining
713 the long term viable development of carbonated mineral waters of Hepburn, Victoria. In *Proc.*
714 *Nation. Env. Conf. Brisbane.*

715 Vandenberg, A. (1978) The Tasman fold belt system in Victoria. *Tectonophysics* 48, 159–205.
716 doi:10.1016/0040-1951(78)90118-x

717 Vollmer, F.W. (2015) Orient 3: a new integrated software program for orientation data analysis,
718 kinematic analysis, spherical projections, and Schmidt plots. *Geol. Soc. Amer. Abstracts with*
719 *Programs* 47 (7), 49.

720 Verdon, J. P., Kendall, J.-M., Stork, A. L., Chadwick, R. A., White, D. J., and Bissell, R. C. (2013)
721 Comparison of geomechanical deformation induced by megatonne-scale CO₂ storage at Sleipner,
722 Weyburn, and In Salah: *Proc. Nat. Acad. Sci.* 110 (30), E2762-E2771. doi: 10.1073/pnas.1302156110

723 Weatherzone (2017) Ballarat Ap Observations. Accessed on 02/08/17.
724 <http://www.weatherzone.com.au/station.jsp?lt=site&lc=89002&list=ob>

725 Weaver, T.R., Cartwright, I., Tweed, S.O., Ahearne, D., Cooper, M., Czapnik, K., Tranter, J. (2006)
726 Controls on chemistry during fracture-hosted flow of cold CO₂-bearing mineral waters, Daylesford,
727 Victoria, Australia: Implications for resource protection. *App. Geochem.* 21, 289–304.
728 doi:10.1016/j.apgeochem.2005.09.011

729 Wishart, E., Wishart, M. (1990) The spa country: A field guide to 65 mineral springs of the Central
730 Highlands, Victoria. Spa Publishing, Daylesford.

731